The effects of asteroid layering on ejecta mass-velocity distribution and implications for impact momentum transfer

S. D. Raducan[a], T. M. Davison[a,], G. S. Collins[a,]

[a]*Impacts and Astromaterials Research Centre, Department of Earth Science and Engineering, Imperial College London, SW7 2AZ, United Kingdom*

Abstract

Most bodies in the Solar System do not have a homogeneous structure. Understanding the outcome of an impact into regolith layers of different properties is especially important for NASA's Double Asteroid Redirection Test (DART) and ESA's Hera missions. Here we used the iSALE shock physics code to simulate the DART impact into three different target scenarios in the strength regime: a homogeneous porous half-space; layered targets with a porous weak layer overlying a stronger bedrock; and targets with exponentially decreasing porosity with depth. For each scenario we determined the sensitivity of crater morphology, ejecta mass-velocity distribution and momentum transferred from the impact for deflection, $\beta-1$, to target properties and structure. We found that for the homogeneous porous half-space, cohesion and porosity play a significant role and the DART impact is expected to produce a $\beta - 1$ between 1 and 3. In the two-layer target scenario, the

Email addresses: s.raducan16@imperial.ac.uk (S. D. Raducan), thomas.davison@imperial.ac.uk (T. M. Davison), g.collins@imperial.ac.uk (G. S. Collins)

presence of a less porous, stronger lower layer close to the surface can cause both amplification and reduction of ejected mass and momentum relative to the homogeneous upper-layer case. For the case of DART, the momentum enhancement can change by up to 90%. Impacts into targets with an exponentially decreasing porosity with depth only produced an enhancement in the ejected mass and momentum for sharp decreases in porosity that occur within 6 m of the asteroid surface. Together with measurements of the DART crater by the Hera mission, these results can be used to test the predictive capabilities of numerical models of asteroid deflection.

Keywords: Impact cratering, Ejecta, Numerical simulations, Layering, Kinetic impactor

---

1. Introduction

Impact cratering is a fundamental processes involved in planetary formation. During the excavation stage of crater formation, a large amount of material is ejected ballistically out of the crater as ejecta (Oberbeck, 1975; Housen et al., 1983). Previous laboratory (Housen and Holsapple, 2011) and numerical studies (Jutzi and Michel, 2014; Luther et al., 2018; Raducan et al., 2019) of impact events into homogeneous targets have shown that the speed and mass of ejecta depends sensitively on target material properties, such as cohesive strength, porosity and the coefficient of internal friction. However, most bodies in the Solar System are not homogeneous, as shown by past missions to asteroids, such as the NEAR-Shoemaker (Veverka et al., 2001), the OSIRIS-REx (Lauretta et al., 2019; Walsh et al., 2012) or the Hayabusa missions (Yano et al., 2006; Watanabe et al., 2019), as well as Earth-based thermal infrared observations (Delbo et al., 2014).

The surface material and the substructure varies from one asteroid to another. While the recent flybys to Ryugu and Bennu revealed a very rocky surface, a large sample of the visited asteroids have been observed to be covered by a layer of fine particles, termed regolith, which overlies a much stronger bedrock substrate (Gundlach and Blum, 2013). Examples of such asteroids include 21 Lutetia (Coradini et al., 2011), 243 Ida, 433 Eros, 951 Gaspra (Sullivan et al., 2002) or 25143 Itokawa (Miyamoto et al., 2007).

The effects of target layering on impact cratering were studied extensively through laboratory experiments conducted by Quaide and Oberbeck (1968). They investigated cratering in analog lunar regolith of different thicknesses, covering a denser, stronger substrate. The study concluded that for a certain

size-range of craters, the depth of the regolith has a large influence on the crater morphology and on the cratering efficiency. For the same impact parameters, a deeper regolith resulted in larger craters (Quaide and Oberbeck, 1968).

The presence of a substrate has also been shown to change the mass-velocity distribution and evolution of ejecta (Schultz, 1992; Senft and Stewart, 2007), which could have important implications for planetary defence, e.g. asteroid deflection by a kinetic impactor (Ahrens and Harris, 1992; Melosh et al., 1994; Shafer et al., 1994). The outcome of an impact into regolith layers of different properties and depths is especially important to understand in the context of space missions such as NASA's Double Asteroid Redirection Test (DART) (Cheng et al., 2016; Cheng et al., 2018) and ESA's Hera (Michel et al., 2018).

In our previous work, Raducan et al. (2019), we presented numerical simulations of strength-dominated impacts on a homogeneous, small-asteroid surface. We quantified the influence of target cohesion, porosity and internal friction coefficient on the mass-velocity ejecta distribution produced by an example artificial impact and used the DART mission (Michel et al., 2016; Cheng et al., 2016) as a motivating case study.

Here, we extend our previous work to include impacts into asteroid surfaces with different internal structures. The paper begins with a brief summary of the DART and Hera missions, a short description of asteroid deflection by momentum transfer and of our current understanding of asteroid surfaces, followed by a summary of past research of impacts into homogeneous and layered targets. We then quantify the effects of the target structure on

crater morphology, the mass-velocity distribution of the ejected material and the amount of momentum transferred from the impactor to the asteroid for deflection. As a layered structure has been proposed for a number of asteroids observed by spacecraft, here we considered three possible impact scenarios: a) a homogeneous half-space target, with constant porosity, b) a layered target with a dense interior, covered by a homogeneously porous regolith layer and c) a target with a porosity that decreases exponentially with depth.

1.1. Kinetic impactor test

To avoid a collision between an asteroid and Earth, the course of the asteroid could be changed by impacting its surface (Ahrens and Harris, 1992; Melosh et al., 1994). The proposed Double Asteroid Redirection Test (DART), set to launch in 2021 (Cheng et al., 2018), aims to demonstrate a controlled deflection of a Near-Earth binary asteroid. The DART mission plans to impact the smaller component of the 65803 Didymos asteroid system, nicknamed Didymoon (Michel et al., 2016), and alter the binary orbit period of the system (Cheng et al., 2018).

In a high velocity impact event, the change in momentum of the asteroid, Δp, can be amplified by the momentum of crater ejecta that exceeds the escape velocity, enhancing the asteroid deflection (Housen and Holsapple, 2011)

$$\Delta p = \beta m v, \tag{1}$$

where m is the impactor mass, v is the impactor velocity and β is the momentum enhancement factor—a measure of the efficiency of momentum transfer. $(\beta - 1)mv$ represents the momentum of the crater ejecta. A value of $\beta - 1 =$

0 implies that the crater ejecta makes no contribution to the total imparted momentum; $\beta - 1 > 1$ indicates that the crater ejecta momentum overall contribution is larger than the momentum imparted from the impactor itself.

The efficiency of momentum transfer has been found to vary significantly depending on the target asteroid's properties and its composition (Holsapple and Housen, 2012; Jutzi and Michel, 2014; Stickle et al., 2015; Bruck Syal et al., 2016). Based on the results of experimental impacts in layered targets (Quaide and Oberbeck, 1968), it is likely that target layering will also affect the mass and velocity of the ejecta, and therefore, β.

To better understand the target properties of Didymoon, ESA is planning a rendezvous mission, Hera (Michel et al., 2018; Cheng et al., 2018), that has a 2023 planned launch and will arrive at Didymoon several years after the DART impact. The Hera spacecraft will provide detailed characterisation of the Didymoon volume and surface properties, as well as measure the outcome of the DART impact, including the new binary system orbit and the volume and morphology of the DART impact crater.

1.2. Lunar regolith

Regolith is defined as a layer of weak of unconsolidated material overlying a stronger substrate (Shoemaker et al., 1963). Most of the lunar regolith is of impact origin (McKay et al., 1991) and consists of particles smaller than 1 cm in size; however, larger fragments or boulders can also be found on the surface. The regolith on the Moon was well characterised in many previous studies (McKay et al., 1991; Wilcox et al., 2005) thanks to the samples returned to Earth from the Apollo missions. The cohesion was measured to

be between 0.1 and a few kPa and the porosity was measured to be 50% (Mitchell, 1974; Colwell et al., 2007), dropping to ≈ 40% in just a few meters. The regolith covers the entire lunar surface and was estimated to be 4-5 m in depth in the mare areas and 10-15 m in the older highland regions (McKay et al., 1991).

1.3. Regolith on Didymoon

The DART mission's target, Didymoon, has a diameter of about 160 m (Michel et al., 2016) and a fast spinning primary close to the critical limit of stability (Walsh et al., 2012). Moreover, like many near-Earth asteroids, the double asteroid system is affected by the YORP effect (Jacobson and Scheeres, 2011).

Small asteroids of about 200 m and up to 10 km in size are likely to be rubble-pile objects (Michel et al., 2001; Richardson et al., 2009), aggregates held together only by self-gravity or cohesive forces (Richardson et al., 2002), while fast-spinning asteroids smaller than 150 m can be competent bodies (Sánchez and Scheeres, 2014). Regardless of the deep internal structure, the surface of many asteroids is expected to be covered by a layer of regolith (Sullivan et al., 2002), but its properties can differ from those of the lunar regolith, as well as from one asteroid to another. The thickness of the regolith layer and the particle size distribution can depend on the size of the asteroid or the internal structure (e.g. a porous asteroid would retain more regolith than a competent body of the same mass).

For example, the high escape velocity on asteroid 21 Lutetia, ≈ 99 km in diameter, has allowed a significant amount of the crater ejecta to be retained on the surface (Murdoch et al., 2015), creating an extensive regolith layer,

similar to the lunar regolith, of up to 600 m in depth (Vincent et al., 2012). Asteroid 433 Eros, $\approx$ 17 km in diameter, has a regolith with particle sizes ranging from dust grains to large boulders, which extend to depths of up to several tens of meters (Veverka et al., 2001; Cheng et al., 2002). Most interesting of all is the 300 m asteroid NEA (25143) Itokawa. Itokawa is believed to be a rubble-pile asteroid (Fujiwara et al., 2006), and has two types of surface terrains: a boulder-rich terrain, with particles larger than 1 cm, and a smooth terrain, with a 2.5 m layer of fine regolith particles covering a boulder rich substrate (Barnouin-Jha et al., 2008).

On the other hand, more recent space missions to top-shaped asteroids—e.g., JAXA's Hayabusa2 to the 435 m Ryugu (Watanabe et al., 2019) and NASA's OSIRIS-REx to the 268 m Bennu (Lauretta et al., 2019; Walsh et al., 2019)—have revealed boulder rich, almost regolith-free surfaces. However, until the arrive of DART at the Didymos system, the surface and internal structure of Didymoon will not be known. Depending on the formation mechanisms involved (Durda et al., 2004; Walsh et al., 2008), Didymoon could be a highly porous fractured body, a regolith-free rubble-pile (like Ryugu and Bennu); it could have a solid intact interior (e.g. a competent or monolithic body), or it could have a layered structure (like Lutetia, Eros or Itokawa) (Scheeres et al., 2010; Sánchez and Scheeres, 2014; Murdoch et al., 2017). In this paper we investigate impacts into a variety of simple internal structures, where the target properties vary only with depth, as possible near-surface structures for Didymoon.

1.4. Impact studies on layered targets

Several previous studies have investigated impacts into layered targets and the resulting crater formation. Oberbeck and Quaide (1967) studied fresh craters, with diameters less than 250 m, on the lunar maria and found four distinct crater morphologies: concentric, flat-bottomed, with a central mound and bowl shaped. They used laboratory impact experiments to determine the impact conditions responsible for each crater morphology occurrence. In their experiments, they set up a simple two-layer target model, consisting of a loose quartz sand upper layer, overlying a substrate of denser cohesive quartz sand cemented with epoxy resin. The layered target was then impacted by various projectiles at velocities between 1 and 7 km/s. Oberbeck and Quaide (1967) were able to reproduce each of the observed crater morphologies by varying the thickness of the upper target layer. The pre-impact layer thickness that produced each crater type was shown to be influenced by the strength ratio of the target layers (Quaide and Oberbeck, 1968), but did not seem to change with variations in the impact velocity, the angle of impact or projectile type.

Senft and Stewart (2007) performed numerical simulations of vertical impacts into basalt two-layer targets on the Moon, where the impact velocity was 17 km/s and the upper layer was 10 m thick. They varied the projectile radius to produce different crater sizes and replicated the Quaide and Oberbeck (1968) crater types. The layered targets had different strength parameters configurations (e.g. cohesion, coefficient of internal friction), which were found to strongly influence the ejecta curtain.

Prieur et al. (2018) also conducted numerical studies of impact crater formation in two-layer targets under lunar conditions and investigated the conditions under which the crater morphologies defined by Quaide and Oberbeck (1968) were produced. In agreement with Quaide and Oberbeck (1968) and Senft and Stewart (2007), they found that the different types of crater morphology are the result of the variations between the properties in the two layers. However, they also found that the transitions between the different crater morphologies depend on the mass and velocity of the impactor, as well as layer-strength variations, which was not observed by Quaide and Oberbeck (1968).

2. Numerical Model

In this work, we used the iSALE2D shock physics code (Collins et al., 2004; Wünnemann et al., 2006) to numerically simulate impacts into asteroid targets with different internal structures. iSALE2D is a multi-material, multi-rheology extension of the SALE hydrocode (Amsden et al., 1980), developed to simulate high-speed impact processes and is similar to the older SALEB hydrocode (Ivanov et al., 1997; Ivanov and Artemieva, 2002). To mimic the material response of an asteroid surface, we used strength models suitable for impacts into geologic targets (Collins et al., 2004) and a porosity compaction model, the $\epsilon - \alpha$ model (Wünnemann et al., 2006; Collins et al., 2011), both of which are included in iSALE2D.

Craters and ejecta distributions produced by impacts simulated with iSALE have been validated previously against laboratory impact experiments (Wünnemann et al., 2016; Luther et al., 2018; Raducan et al., 2019). iSALE

has also been benchmarked against other hydrocodes (Pierazzo et al., 2008), with crater size typically agreeing to within 10%.

2.1. Impactor

The impactor parameters were chosen to approximate the DART spacecraft. We assumed a 310 kg porous sphere, with a diameter of 0.84 m, modelled using the Tillotson equation of state (EOS) and the Johnson-Cook strength model for aluminium (Johnson and Cook, 1983). The internal structure of the spacecraft was heavily simplified and we used the $\epsilon - \alpha$ porosity model (Wünnemann et al., 2006) to account for the voids in the spacecraft structure and achieve a bulk density of 1000 km/m^3 (63% bulk porosity). The $\epsilon - \alpha$ model took the nominal input parameters: $\alpha_0 = 2.7$, $\alpha_x = 1.0$, $\kappa = 0.9$, $\chi = 1.0$. To isolate the influence of target properties, we used the same impactor properties and an impact velocity of 7 km/s for all simulations.

2.2. Target asteroid

As discussed in the previous section, Didymoon's surface properties or internal structure are not well understood. To study the target material response to a possible impact, we numerically simulated impacts into three distinct target scenarios: (a) a homogeneous porous half-space (Fig. 1a); (b) a layered target with a porous weak upper layer overlying a stronger bedrock layer (Fig. 1b); and (c) a target with a porosity that decreased exponentially with depth (Fig. 1c). For each of these target scenarios we systematically varied the target material properties (e.g. cohesive strength, initial porosity – including crush curve, layer thickness or porosity e-folding

depth) and determined the crater morphology, the amount of ejected mass and the normalised momentum carried away by the ejecta, $\beta - 1$.

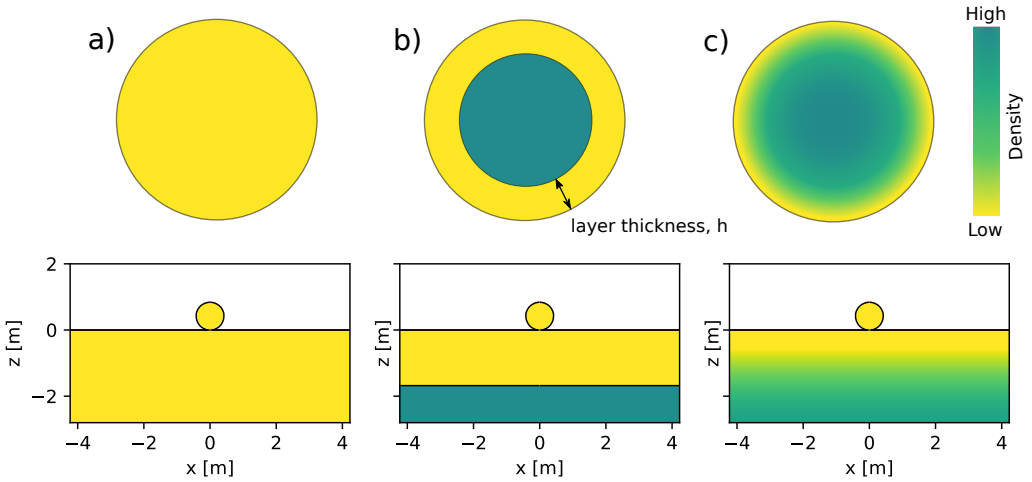

Figure 1: Schematic representation of the asteroid structure (upper row) and the equivalent numerical simulation set-up (lower row), for: a) homogeneous porous half-space; b) layered target consisting of a weak, porous upper layer covering a stronger, less porous substrate; c) target with a continuous porosity gradient.

As an S-type silicaceous asteroid system (Michel et al., 2016; Michel et al., 2018), the target asteroid material was considered to be made of weak porous basalt, which is a reasonable approximation of the compositional structure of most asteroids. Therefore, for all impact scenarios, the target was modelled using the Tillotson EOS for basalt (Tillotson, 1962; Benz and Asphaug, 1999). The surface gravity was kept constant at 5×10^{-3} cm/s^2.

2.2.1. Homogeneous porous half-space

The first scenario investigated DART impacts into a homogeneous porous half-space. The shear strength of the target was modelled using a simple

pressure-dependent strength model typical of rock-like materials, referred in this paper as LUND (Lundborg, 1967). The cohesive strength of the damaged target (at zero pressure), Y_{d0}, was varied between 0.1 and 100 kPa. The coefficient of internal friction, f, which can take a range of values on asteroid surfaces, was set to 0.6. This value was based on geological analogues and is the most common for geological materials (Goodman, 1989).

The initial porosity of the target, ϕ_0, was varied between 0% and 50%, and was modelled using the $\epsilon-\alpha$ model (Wünnemann et al., 2006). The input parameters for the $\epsilon - \alpha$ model (Table 1) were derived from mesoscale modelling studies of dynamic compaction of chondritic material (Davison et al., 2016) and informed by comparison with measured crush curves (distension as a function of pressure) of analog materials (Fig. 2). We favoured the synthetic dynamic crush curves because they provide a systematic framework for varying all of the compaction model parameters over the range of target porosities considered here. Moreover, without crush-curve measurements of a direct sample of asteroid surface material it is difficult to determine the best analog for the compaction behaviour of asteroidal materials. Proposed asteroid regolith analogs, including gypsum (Nakamura et al., 2009), sand (Hagerty et al., 1993; Housen et al., 2018) and lunar regolith (Stephens and Lilley, 1970; Ahrens and Cole, 1974), show a range of compaction behavior. One way to characterise the compaction response is by a "crushing strength" defined as the pressure required to compact the material by one-half towards its solid density (Housen et al., 2018). For an initial porosity of 20% and 35% the crush curves used in this work are broadly consistent with the quasi-static crush curves of lunar microbreccia and lunar regolith (Fig. 2), and have sim-

ilar crushing strengths (Stephens and Lilley, 1970; Ahrens and Cole, 1974). The crushing strengths in our iSALE simulations were ≈ 450-650 MPa for 35% - 20% initial porosity, while the lunar regolith and the lunar microbreccia have crushing strengths of ≈ 420 MPa and 800 MPa, respectively. For an initial porosity of 35% and 50% the crush curves at low pressures are also broadly consistent with the crush curves of sand (Hagerty et al., 1993; Housen et al., 2018) and gypsum (Nakamura et al., 2009), respectively (Fig. 2). However, both of these earth-sourced analogs have crushing strengths that are somewhat lower than those of the lunar analogs, perhaps because lunar regolith grains are more angular with a higher internal friction angle than their terrestrial counter parts. Nevertheless, we note that in our simulations only a very small fraction of the (high velocity) ejecta experiences pressures above 100 MPa, so we do not expect our results to be very sensitive to uncertainty in the high-pressure portion of the regolith crush curve. A small number of test simulations showed that adopting a lower crushing strength for a uniform regolith target changes the $\beta - 1$ value by less than 4%.

The elastic volume strain threshold ϵ_{e0} defines the volume strain that must be exceeded to induce permanent compaction. It can be converted to an approximate pressure at the onset of crushing by multiplying by the bulk modulus. As in previous work (Raducan et al., 2019), ϵ_{e0} was set proportional to the ratio of the cohesion of the damaged material Y_{d0} and the bulk modulus. For simplicity and numerical stability, we set the χ parameter (the elastic wave speed ratio of porous and non-porous material) to 1, implying that the elastic wave speed in the porous material was equal to that in the nonporous component. In reality, the elastic wave speed in a porous material

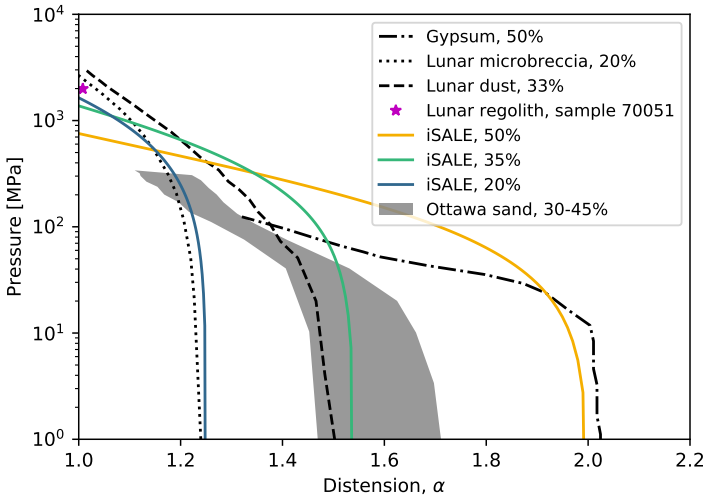

Figure 2: Crush curves used in iSALE for homogeneous targets with 20%, 35% and 50% porosity, compared with experimentally derived, quasi-static crush curves for 50% porous gypsum (Nakamura et al., 2009), 30-45% porous Ottawa sand (shaded area) (Hagerty et al., 1993; Housen et al., 2018), lunar dust and lunar microbreccia (Stephens and Lilley, 1970). Also shown is the result of one shock compaction experiment for lunar regolith (sample 70051) (Ahrens and Cole, 1974). To convert bulk density to distension, α is estimated as the ratio of reference grain density to compressed bulk density, ρ_{s0}/ρ.

is usually only a small fraction of the speed in the solid component; however, sensitivity studies showed that for the scenarios simulated here, the χ parameter has a negligible effect on crater formation, ejected mass or ejection speeds. This is because inside the crater the stress wave is still in the plastic/shock regime and its speed is dictated primarily by the crush curve (and solid equation of state), rather than the elastic wave speed.

Table 1: Material model parameters for simulations of the DART impact. In addition, thermal parameters from Ivanov et al. (2010) were used.

Description	Symbol	Half-space	Regolith	Substrate
Equation of state		Tillotson[a]	Tillotson[a]	Tillotson[a]
Strength model		LUND	LUND	ROCK
Poisson ratio[b]	ν	0.25	0.25	0.25
Intact strength at zero pressure (MPa)	Y_{i0}	–	–	1
Damage strength at zero pressure (kPa)	Y_{d0}	0.1–100	1	100
Strength at infinite pressure (MPa)	Y_{inf}	10^3	10^3	10^3
Coefficient of internal friction (intact material)	f_i	–	–	1.0
Coefficient of internal friction (damaged material)	f	0.6	0.6	0.6
Porosity model parameters $(\epsilon - \alpha)^c$				
Initial porosity	ϕ_0	0–50%	35%/50%	0%/10%
Initial distension**	α_0	1.0–2.0	1.54/2.0	1.0/1.11
Distension at transition to power-law	α_x	1.0	1.0/1.0	– /1.0
Elastic volumetric strain threshold*	ϵ_{e0}	-2×10^{-9}–-2×10^{-6}	-2×10^{-8}	–/-2×10^{-6}
Exponential compaction rate**	κ	0.80–0.98	0.94/0.98	– /0.80
Ratio of porous/nonporous elastic wave speed	χ	1.0	1.00/1.00	– /1.00

[a] Tillotson (1962); [b] Ivanov et al. (2010); [c] Wünnemann et al. (2006).

* ϵ_{e0} varies proportionally with Y_{d0}.

** $\alpha_0 = 1/(1 - \phi_0)$ and κ vary with ϕ_0.

2.2.2. Two-layer targets

The second impact scenario considered a simple two-layer target structure, consisting of a weak, porous upper layer covering a stronger, less porous substrate. This target scenario is similar to what is observed on the Moon. To quantify the effects of target layering on the crater morphology and ejecta, we considered four sets of simulations, with different layer porosity configurations.

For all simulation sets, both the upper and the lower target materials were modelled using the Tillotson EOS for basalt. The upper layer had a cohesive strength of 1 kPa and was modelled using the LUND strength model (Lundborg, 1967), while the lower layer had a cohesive strength of 100 kPa and was modelled using a more complex strength model, in which the strength is reduced as strain accumulates (Collins et al., 2004), referred

in this paper as the ROCK model. Senft and Stewart (2007) showed that at least a two-orders-of-magnitude difference between the strength in the upper layer and the substrate is required in order to produce different crater morphologies. Both layers had a coefficient of internal friction of the damaged material $f = 0.6$, while the coefficient of internal friction of the intact material (only in the ROCK model) was set to $f_i = 1.0$.

We performed four sets of simulations. For each set of simulations we varied the porosity in the upper and lower layers. In the first two sets, the upper layer (the regolith) had a nominal porosity of 35% and 50%, respectively, while the lower layer (the substrate) was non-porous (0% porosity). These two simulations will be referred to as R35-S0 and R50-S0 (Table 3). The next two sets considered less extreme variation in porosity between the regolith and substrate. In these two cases the regolith was 35% and 50% porous, respectively, while the substrate had a porosity of 10%. These simulation sets were labelled R35-S10 and R50-S10. The full range of input parameters can be found in Table 1 and a summary of the simulation sets can be found in Table 3.

To investigate the influence of the regolith layer on the crater morphology and the ejecta produced, for each set of simulations we varied the regolith layer thickness, h, between 1 and 20 impactor radii.

Table 2: iSALE input parameters for the layered target.

Parameter	R35-S0	R50-S0	R35-S10	R50-S10
Regolith porosity, ϕ_{r0}	35%	50%	35%	50%
Substrate porosity, ϕ_{s0}	0%	0%	10%	10%

2.2.3. Targets with exponentially decreasing porosity

As noted by Sullivan et al. (2002), the transition between regolith and megaregolith on asteroids might not be as sharp as on the Moon, but instead might be more gradual. The third target scenario considered a target in which porosity decreased exponentially with depth. In all cases, strength was assumed to be independent of porosity and modelled using the LUND strength model with a fixed cohesive strength and coefficient of friction (Y_0 = 1 kPa and $f = 0.6$). In iSALE, the distension, α, is defined as the ratio of solid density to bulk density, ρ_s/ρ, which is equivalent to $1/(1-\phi)$, where ϕ is the porosity (Collins et al., 2011). To achieve an exponential decrease in porosity with depth, the distension as a function of depth, $\alpha(h)$, is defined as

$$\alpha(h) = (\alpha_0 - \alpha_k) \times \exp(h/h_\star) + \alpha_k \tag{2}$$

where α_0 is the distension at the surface (maximum distension), α_k is the minimum distension (asymptotic limit), h is the depth and $h_\star$ is the e-folding depth. For this impact scenario, the $\epsilon - \alpha$ parameters were kept constant for all initial distensions, including the critical volume strain for the onset of

plastic compaction, ϵ_{e0}.

To investigate impacts into targets with exponentially decreasing porosity, we considered two simulation sets. The fist set had a surface porosity, ϕ_0, of 50% and a minimum porosity, ϕ_k, of 0%, while the second set had $\phi_0 = 35\%$ and $\phi_k = 10\%$. For each set, we varied the e-folding depth, $0.12 < 1/h_\star < 1.2$.

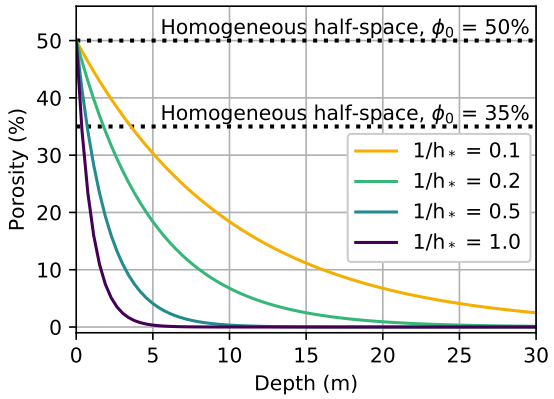

Figure 3: Target porosity as a function of depth for a range of values $1/h_*$, between 0.12 and 1.2. The surface porosity is 50% and the minimum porosity is 0%. The porosity in homogeneous half-space cases, at 35% and 50% porosity, are plotted for comparison.

Table 3: iSALE input parameters for the porosity gradient target.

Parameter	S50-K0	S35-K10
Surface porosity, ϕ_0	50%	35%
Minimum porosity, ϕ_k	0%	10%

2.3. Regridding and resolution tests

High spatial resolution is required to capture the particles ejected at very high velocities in the early stages of impact. At the same time, in all of our simulations the crater grows to become many times larger than the projectile and cratering occurs over a long time-scale, due to the low gravity and low strength of the targets investigated. To achieve high spatial resolution at early times, whilst limiting the computational expense of simulations, we used the iSALE's regridding option. Regridding allowed the simulation domain to be coarsened by a factor of two after predetermined amounts of time. This method produced results that were comparable to those from simulations using 40 cells per projectile radius (cppr) resolution, but at an approximately equivalent cost of a 5 cppr run (Raducan et al., 2019).

Lagrangian tracer particles were placed across the computational domain and their mass and velocity were recorded if they crossed a fixed altitude, equal to one impactor diameter. Tracers that crossed this line were identified as ejecta in post-processing if their maximum speed exceeded both the escape velocity (≈ 6 cm/s) and the velocity required to overcome the cohesive strength of the target. In all cases considered here, the velocity threshold was 10 cm/s. Due to the very small size of the simulated asteroid, the ejecta analysis presented here ignored the effect of gravity on the absolute value of the ejecta velocity at infinity (Housen and Holsapple, 2003). The gravity of Didymoon, albeit small, would affect the slower ejecta, which introduces an uncertainty in β of 2 to 4%.

The numerical simulations were run until all the ejecta was measured, however it is important to note that the end of the simulation was not neces-

sarily the end of the cratering process. Further crater collapse, which due to the very low surface gravity occurs over a much longer time-scale than crater excavation, was not simulated.

3. Results of the DART impact

To understand and quantify the effects of target structure on the crater morphology, amount of ejected mass and ejecta momentum, we divide our numerical studies into three different impact scenarios.

3.1. DART impact into a homogeneous porous half-space

To investigate the individual effects of target cohesion and porosity on crater excavation and ejection processes, we first performed a series of simulations of impacts into homogeneous half-space targets. This extended results presented in Raducan et al. (2019), by providing additional numerical runs that covered a larger range of target porosities.

To investigate the effects of target cohesion we varied Y_{d0} between 0.1 and 100 kPa, while keeping the porosity set at 20% and all the other impact parameters constant. We found that the target cohesion had a large influence on the crater diameter at the preimpact surface level, which varied from 36 m for a 0.1 kPa target, to 9 m at 100 kPa.

To investigate the effects of porosity at constant cohesion, we varied the porosity between 0% and 50%, for cohesions of 1, 10 and 100 kPa. For all cohesions, the crater diameter decreased by about one third between the non-porous and 50% porosity target scenarios. However, the relative change in crater diameter between the 20% and the 50% porosity targets was less than 2 m (8-14%), which might be difficult to resolve from images taken

by a potential post-impact fly-by. This relatively modest change in crater diameter with porosity is consistent with previous experiments (Housen and Holsapple, 2003) and numerical simulations (Wünnemann et al., 2006; Prieur et al., 2017) of impacts in low-to-moderate porosities (up to 50%). A greater dependence of crater diameter and depth on crater size is expected for higher porosity targets not considered here (Housen and Holsapple, 2003).

By analysing the impact ejecta, we found that an increase in target porosity led to lower ejection velocities, while an increase in target cohesion resulted in lower ejection speeds only for the last ejecta to leave the crater. This is consistent with the results of recent numerical simulations of ejecta behaviour in gravity-dominated impacts (Luther et al., 2018).

By integrating the mass-velocity ejecta distribution, we determined the momentum transferred to the target and carried away by the ejecta, $\beta - 1$. Our simulation results suggest that $\beta - 1$ is also very sensitive to the material properties investigated, with the target cohesion having the greatest influence. Figure 4 shows the the ratio of ejected momentum to impactor momentum $\beta - 1$, as a function of target porosity, for four different cohesions. As the cohesion is decreased, $\beta - 1$ increases; $\beta - 1$ also increases as the initial porosity of the asteroid surface decreases. For a target with 20% porosity, which is the current best estimate for the Didymos asteroid system (Michel et al., 2016), $\beta - 1$ was determined to range between 1 for a cohesion of 100 kPa and approximately 3 for a cohesion of 0.1 kPa.

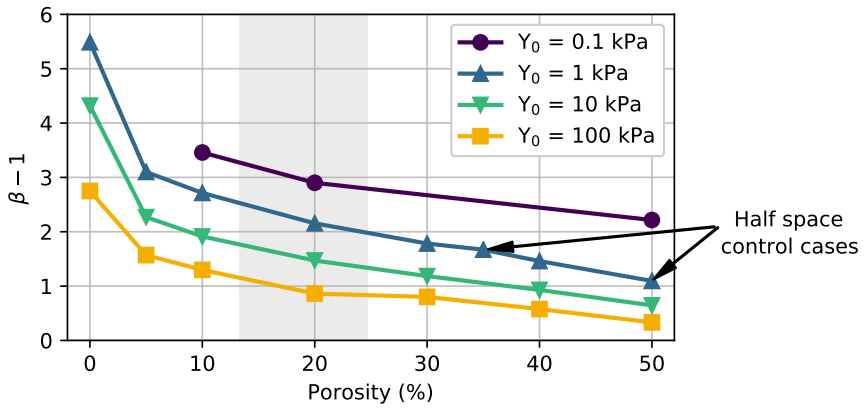

Figure 4: Total ejected momentum in the z direction ($\beta - 1$) for four different cohesions and different porosities of the target. Adapted from Raducan et al. (2019).

Our results are broadly consistent with previous impact simulations where targets with similar cohesive strengths were used. For example, simulations by Bruck Syal et al. (2016) suggested a 10 km/s impact into a 1 kPa, 20% porous target would produce a $\beta - 1 \approx 3$, while impacts into much stronger targets, of a few MPa, have been shown to produce $\beta - 1$ between 0.1 and 1 (Jutzi and Michel, 2014; Stickle et al., 2015; Cheng et al., 2016)). As discussed in Raducan et al. (2019), these results emphasise the importance of cohesion in determining the β value and the outcome of asteroid deflection.

3.2. DART impact into a two-layer target

We performed four sets of numerical simulations of impacts into layered Didymoon-like targets, where each set had a different porosity configuration in the upper and lower layers, as summarised in Table 3. For each simulation set we varied the thickness of the regolith, h, from 0.5 to 20 times the

impactor radius, a.

3.2.1. Crater morphology

Varying the upper-layer thickness resulted in craters with different morphologies. We identified the same four types of crater morphologies as reported by Quaide and Oberbeck (1968): concentric craters, flat-floor craters, central-mound craters and bowl shaped craters. Examples of crater profiles of these morphologies, from our iSALE simulations, are illustrated in Fig. 5. The crater profiles are recorded at the end of the crater growth process ($\approx$ 10 s); however, the material velocity in the rim area is non-zero and directed inwards at this time. This suggests that further collapse of rim material might occur, but over a long timescale due to the low gravity of the body. In Fig. 5, the material with a particle velocity pointing downwards and that might collapse is highlighted in red.

For very thin regolith layers, h/a <4, cratering deformed both the upper and the lower layers, to produce concentric craters with both an inner and outer crater rim. As the regolith layer was increased, in the range 4< h/a <10, the same impact conditions produced a crater that only formed into the upper layer and exhibited a flat floor. For regolith layer thicknesses h/a between 10 and 16, the impact produced central-mound craters, while for very thick regolith layers, $h/a > 16$, the substrate had no influence on the cratering process. In this case, the crater took the form of a simple bowl shaped crater, similar to the craters formed in the equivalent homogeneous target simulation.

In our study, the transition threshold between these crater morphologies did not appear to be influenced by the range of porosities investigated. How-

ever, Prieur et al. (2018) noted the the transition threshold between crater morphologies, for a given impact into a layered target, depended on the impactor's mass and velocity.

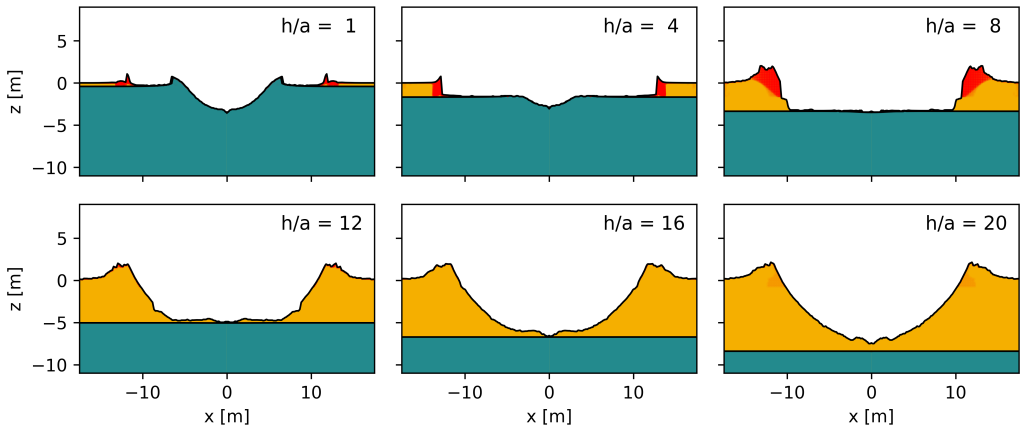

Figure 5: Example of crater profiles with distinct morphologies: concentric crater (h/a = 1), flat-bottomed (h/a = 8), central-mound (h/a = 12) and bowl shaped (h/a = 20). The upper layer had a pre-impact porosity of 35%, while the substrate was non-porous. Crater rim material highlighted in red is expected to undergo late-stage collapse.

3.2.2. Ejected mass

We have shown in the previous section that DART impacts into two-layer targets produce different crater morphologies, each of which had a different cratering efficiency. For impacts into homogeneous targets, the crater size is strongly correlated with the amount of ejecta produced, and a similar behaviour is expected for impacts into layered targets.

Fig. 6 shows the total ejected mass, M, as a function of the upper layer thickness, normalised by the impactor radius, h/a. The ejected mass for each simulation is normalised by the amount of ejected mass from an equivalent

impact into a half-space regolith target, with no lower layer, M_{hs}. R35-S0 and R35-S10 results are normalised by the total mass ejected from an impact into a 35% porosity homogeneous half-space target, while R50-S0 and R50-S10 results are normalised by the mass ejected from an impact into 50% porosity half-space target.

For impacts into regolith layers with a thickness greater than $\approx 18\ h/a$, the total ejected mass converged to the mass ejected in the equivalent homogeneous regolith scenario. As the crater only formed in the upper layer, the influence of the substrate on the excavation flow was not significant. However, as the substrate got closer to the surface, up to 20% more mass was ejected than in the porous homogeneous regolith cases. This amplification in ejected mass is a consequence of the difference in the mechanical impedance (the product of density and wave speed) between the upper and lower layers. The impedance contrast results in a strong reflection of the shock wave at the boundary, and only partial transmission of energy into the substrate. As a result, less of the impactor kinetic energy was transmitted into the substrate and more was retained within the shallow subsurface, which amplified the ejection speeds in the upper layer.

On the other hand, for thin regolith layers (h/a less than 4; concentric craters) the ejected mass is less than in the homogeneous upper-layer case, despite the greater density of the material in the lower layer. At these regolith thicknesses, the excavation flow is strongly impeded at depth by the higher strength in the lower layer, but less impeded in the weaker regolith. The large strength difference between the layers more than compensates for the higher density of the substrate material and results in a reduction in total

ejected mass relative to the homogeneous upper-layer case.

For intermediate regolith layer thicknesses of about $4 < h/a < 10$, the total ejected mass can be higher or lower than in the homogeneous upper-layer case, depending on the size of the porosity contrast between the layers. In this regime, both effects— increased resistance to flow in the substrate, and reflection of kinetic energy back into the regolith—are in competition. For the scenarios with a nonporous substrate, maximum ejecta mass amplification (20-30%) occurs at a regolith thickness of $h/a \approx 6$. A small amount (10%) of porosity in the substrate material is sufficient to negate most of the amplification of ejection from shock wave reflection.

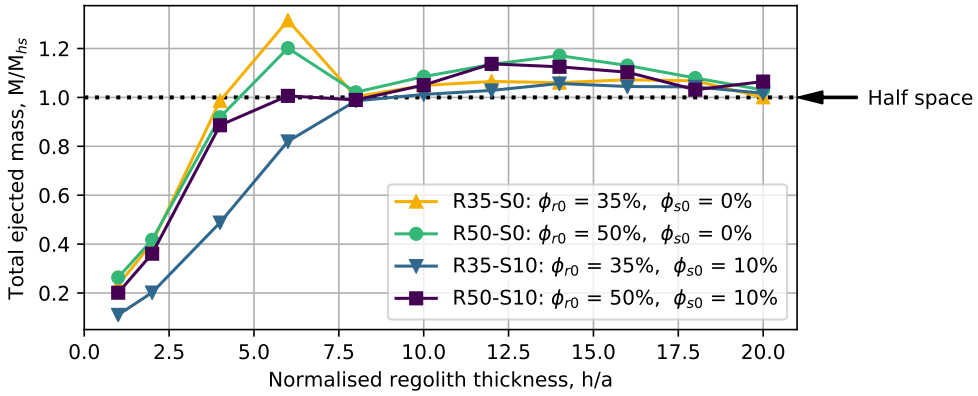

Figure 6: Total ejected mass, M, normalised by the mass ejected in the half-space case, M_{hs}, for impacts into layered targets with different regolith-substrate porosities configurations: R35-333S0, R50-S0, R35-S10 and R50-S1 (see Table 3 for details). The total mass is plotted as a function of regolith thickness h normalised by the impactor radius, a.

3.2.3. Ejected momentum

Fig. 7a shows the cumulative mass ejected at speeds higher than velocity v, $M(> v)$, normalised by the mass of the impactor, m, as a function of ejec-

tion velocity, v, normalised by the impactor velocity, U. The cases illustrated are for a 35% porosity upper layer and a nonporous substrate (R35-S0). The ejecta mass-velocity distributions were integrated to determine the cumulative, vertically ejected momentum, $p_{ej(z)}/mU = (\beta - 1)$, as a function of ejection speed in the vertical direction v_z (Fig. 7b).

An impact into a 35% porous homogeneous regolith target produced a normalised total ejecta momentum, $\beta - 1$, of about 1.75 (y-intercept of the dotted line in Fig. 7b). The effects of layer thickness on ejected momentum are more complex than on the ejected mass, as layering influences both the velocity and the mass of ejecta. For a regolith layer thickness $h/a = 14$, $\beta - 1$ is $\approx 10\%$ greater than in the regolith half-space case. At this regolith thickness, the top of the substrate is sufficiently close to the surface for the reflected shock wave to significantly increase ejection speeds towards the end of crater growth. This results in the amplification of ejection speeds and momentum of the slowest ejecta that is last to leave the crater.

For regolith thicknesses $4 < h/a < 10$, where the impact formed flat-floored craters, the shock wave reflects off the regolith-substrate boundary earlier in the cratering process, because the boundary is closer to the surface. Earlier shock wave reflection likewise results in amplification of ejection speeds earlier in the cratering process, such that even the fastest ejecta are given an extra acceleration from the reflected shock wave. For $h/a \approx 6$, $\beta - 1$ is increased to over 2.

For thin regolith layers, $h/a < 6$, a number of competing effects are observed. On the one hand, as regolith thickness is decreased the reflected shock wave occurs earlier and earlier, tending to produce an even larger

amplification of ejection speeds. On the other hand, the high strength of the substrate also acts to retard the excavation flow at depth, which reduces ejection speeds. Finally, as the regolith layer gets very thin, $h/a < 1$, dense, lower layer material becomes part of the ejecta mass. Both the mass and the speed of the fastest ejecta, relative to the porous half-space case, were increased by the high density and the low shock wave attenuation of the lower layer. The highest $\beta - 1$ value was observed in the thinnest regolith layer case simulated, with $h/a = 0.5$.

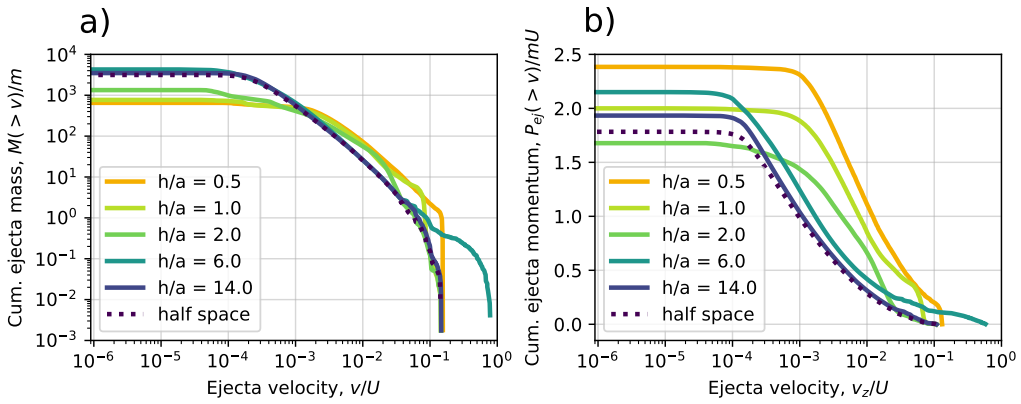

Figure 7: Ejecta distribution from impacts into layered target with a 35% porosity regolith of varying thicknesses ($0.5 < h/a < 14$), overlying a non-porous substrate. a) Cumulative ejected mass, $M(> v)$, normalised by the mass of the impactor, m, as a function of normalised ejection velocity, v/U. b) Total ejected momentum, $\beta - 1$, as a function of the normalised vertical component of the velocity, v_z/U.

Fig. 8 shows the momentum carried away by the ejecta, $\beta - 1$, as a function of regolith thickness, h/a, for the four layering scenarios investigated here: R35-S0, R50-S0, R35-S10 and R50-S10. For thick regolith layers, the trend in all cases is well behaved, while for thinner regolith layers, h/a <10, the

behaviour is more complex. In this range, $\beta - 1$ is very sensitive to the material properties of the two layers. The figure also shows that when the substrate has a small porosity, any amplification in ejected momentum is reduced or even negated for thin-layer scenarios.

Compared with the uniform half-space cases, we found that the optimum layer thickness that produces the maximum ejected momentum depends on the strength and density ratios of the two layers, and it can be different to the layer thickness that results in the greatest total ejected mass.

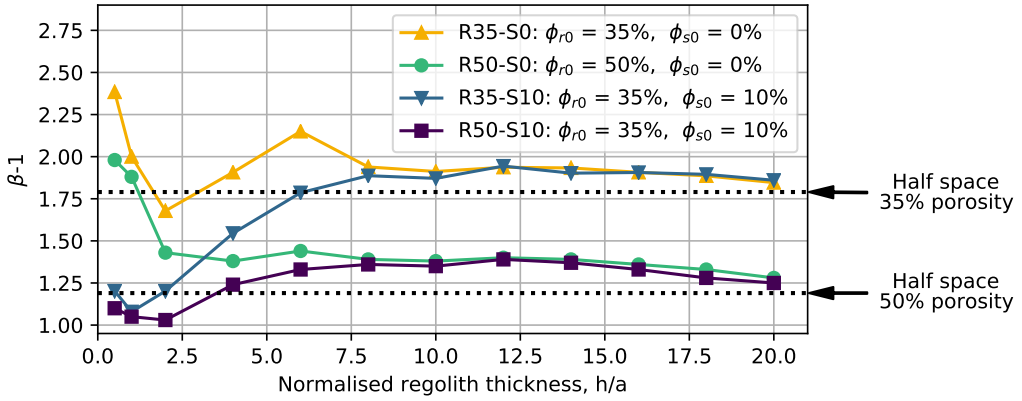

Figure 8: Normalised ejected momentum, β-1, from impact simulations into four different configurations of layered targets, R35-S0, R50-S0, R35-S0 and R50-S10 (Table 3). β-1 is plotted as a function of target regolith thickness, h, normalised by the impactor radius, a. β-1 from impacts into 35% and 50% porous half-space are plotted for comparison (dotted horizontal lines).

In the R35-S0 impact scenario, the most mass was ejected at $h/a = 6$, and the largest $\beta - 1$ amplification was at h/a <0.5, with a 30% amplification, and at $h/a = 6$, with a 20% amplification. On the other hand, in the R50-S0 impact scenario, the most mass was ejected at $h/a = 6$, while

$\beta - 1$ was only 10% larger than in the regolith half-space case. This suggests that the additional mass is ejected at very low velocities and it does not add significantly to the total momentum of the ejecta. The greatest ejected momentum occurred at h/a = 0.5, even though the ejected mass in this case was 70% lower than the homogeneous regolith case.

3.3. DART impact into targets with an exponentially decreasing porosity with depth

The last simulated scenario considered DART impacts into asteroid targets with a porosity that decreased exponentially with depth. We numerically simulated impacts into two target configurations, one with a surface porosity of $\phi_0 = 50\%$ and a minimum porosity of $\phi_k = 0\%$ (S50-K0), and one with surface porosity of $\phi_0 = 35\%$ and a minimum porosity of $\phi_k = 10\%$ (S35-K10). For each target configuration we varied the porosity e-folding depth, $0.1 < 1/h_* < 1.0$.

All the impacts simulated in this case formed simple bowl-shaped craters, with radii that remained almost constant with varying e-folding depth, h_*. The crater radius was ≈10 m in the S50-K0 case and ≈10.5 m in the S35-K10 case, which is comparable to the radius of craters formed in the equivalent half-space targets, with 50% and 35% porosity, respectively.

Fig. 9a shows the total ejected mass for the two simulated scenarios, S50-K0 and S35-K10, as a function of normalised porosity e-folding depth, h_*/a. A smaller e-folding depth implies a more rapid decrease in porosity with depth below the surface (Fig. 9). In both cases, the ejected mass is normalised by the total ejected mass in their corresponding minimum porosity half-space scenario.Fig. 9b shows the total momentum carried away by the ejecta in the

574 z-direction, normalised by the impactor momentum, $\beta - 1$, as a function of
575 normalised porosity e-folding depth, h_*/a.

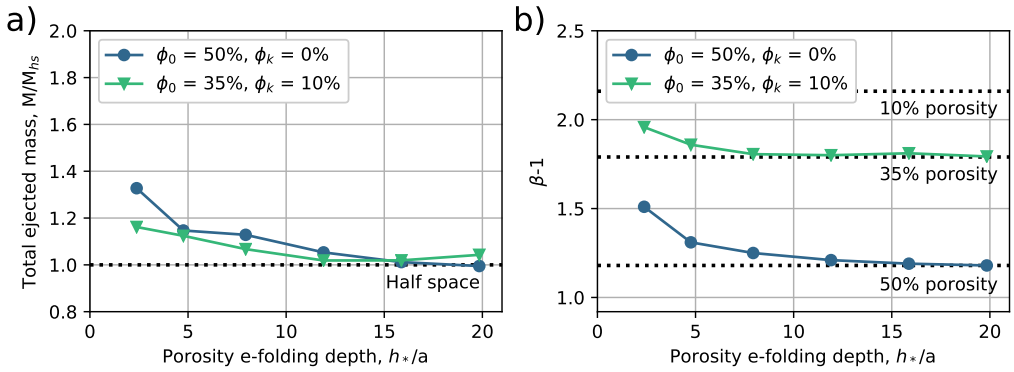

Figure 9: Numerical simulations results for impacts into targets with a continuous porosity gradient. a) Total ejected mass, as a function of normalised porosity e-folding depth, h_*/a. The mass ejected from the ϕ_0=50%, ϕ_k = 0% case was normalised by the 50% half-space scenario and the mass from ϕ_0=35%, ϕ_k = 10% was normalised by the 35% half-space scenario. b) Normalised ejected momentum, $\beta - 1$ as a function of normalised porosity e-folding depth. The dotted horizontal lines represent the $\beta - 1$ in the 10%, 35% and 50% porosity half-space.

576 Both the ejected mass and the ejected momentum graphs follow the same
577 trend. For large porosity e-folding depths, h_*/a >12, there was no significant
578 increase in the ejected mass or the ejected momentum, compared to the
579 equivalent half-space scenario. On the other hand, as porosity e-folding depth
580 decreased, h_*/a <<12, more mass was ejected as the density of the ejected
581 subsurface material increased. Similarly, the denser ejected mass also added
582 to the amount of ejected momentum, $\beta - 1$, causing an amplification of up
583 to 25%.

4. Discussion

4.1. Comparing ejecta from impacts into layered targets with impacts into targets with a porosity gradient

To allow for a meaningful comparison between two impacts, where one is in a layered target and one is in a homogeneous target with exponentially increasing density, we compared the ejecta mass and momentum transfer from impacts into targets with equivalent mass per unit area. We integrated the porosity-target depth function for each simulated target and found that a layered target of thickness h/a has the same mass per unit area as a target with a porosity e-folding gradient of h_*/a. For example, a target with a surface porosity $\phi_0 = 50\%$, minimum porosity $\phi_k = 0\%$ and an e-folding depth of $h_*/a = 20$ had the same integrated area as a target with a $20a$ thick 50% porous regolith layer overlying a non-porous substrate (Fig. 10).

Fig. 11a shows the total ejected mass from the R50-S0 layering scenario (50% porosity upper layer over a non-porous substrate), compared with the S50-K0 porosity gradient scenario (50% surface porosity and 0% minimum porosity). The ejected mass in the layered targets is plotted as a function of regolith layer thickness, h/a, while the ejected mass from the exponentially-decreasing porosity targets is plotted as a function of porosity e-folding depth, h_*/a. Similarly, Fig. 11c shows the normalised ejected momentum, $\beta - 1$ for the R50-S0 layering scenario, compared with the S50-K0 exponentially-decreasing porosity scenario.

Impacts into both the layered target and the exponentially-decreasing porosity target scenarios display an amplification in the amount of ejected momentum, $\beta - 1$, compared to the homogeneous 50% half-space case. In

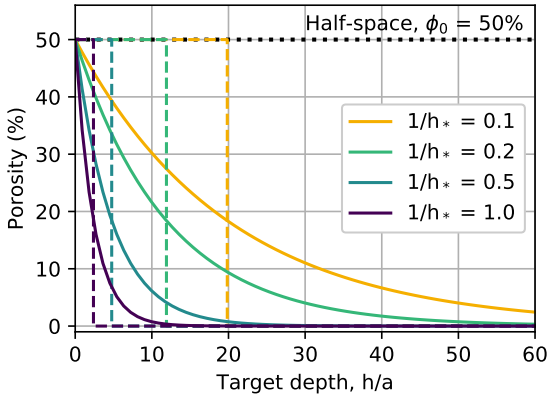

Figure 10: Target porosity as a function of depth for a range of e-folding depths, $0.1 < 1/h_* < 1.0$. The surface porosity is 50% and the minimum porosity is 0%. The equivalent integrated area from a layered target porosity-depth function is shown in same colour and dashed lines. The homogeneous half-space case at 50% porosity is plotted for comparison (dotted line).

both cases, $\beta - 1$ has an ascending trend with decreasing regolith thickness, and with values of up to 60% larger than in the half-space case (Fig. 11c). However, the mechanism responsible for the amplification differs between the two scenarios. For the exponentially-decreasing porosity scenarios, the amplification in $\beta - 1$ is caused by the ejection of denser subsurface material. In the layered scenario, the amount of ejected mass is limited by the high strength of the substrate, which impedes the excavation flow (Fig. 11a). The amplification in $\beta - 1$ is instead caused by the ejecta acceleration due to the reflection of the shock wave.

Fig. 11b and d show the normalised total ejected mass and the normalised ejected momentum from the R35-S10 layering scenario (35% porosity upper layer over a 10% porous substrate), compared with the S35-K10 porosity

gradient scenario (35% surface porosity and 10% minimum porosity).

For $h/a < 10$, impacts into the S35-K10 target scenario produced similar trends for $\beta - 1$ as in the S50-K0 target scenario, with an increased amplification in the amount of ejected momentum towards sharper porosity gradients, compared to an impact into a 35% porous half-space. At the same time, for the same h/a, impacts into R35-S10 produced smaller $\beta - 1$. This is caused by the difference in strength: in the layered case, the lower layer is denser, but also stronger; in the porosity gradient case, the deeper material is denser, but not stronger.

The work presented here is just a first step in understanding the effects of layering on small-body crater formation. Future work is needed to examine the effect of a continuous increase in strength with depth commensurate with the decrease in porosity. Impact angle is also expected to play a significant role in the ejecta distribution and momentum transfer. While numerical simulations presented were restricted to vertical impact only, future studies should also investigate and quantify the role of the impact angle on the ejecta distribution of impacts into homogeneous and layered asteroid targets.

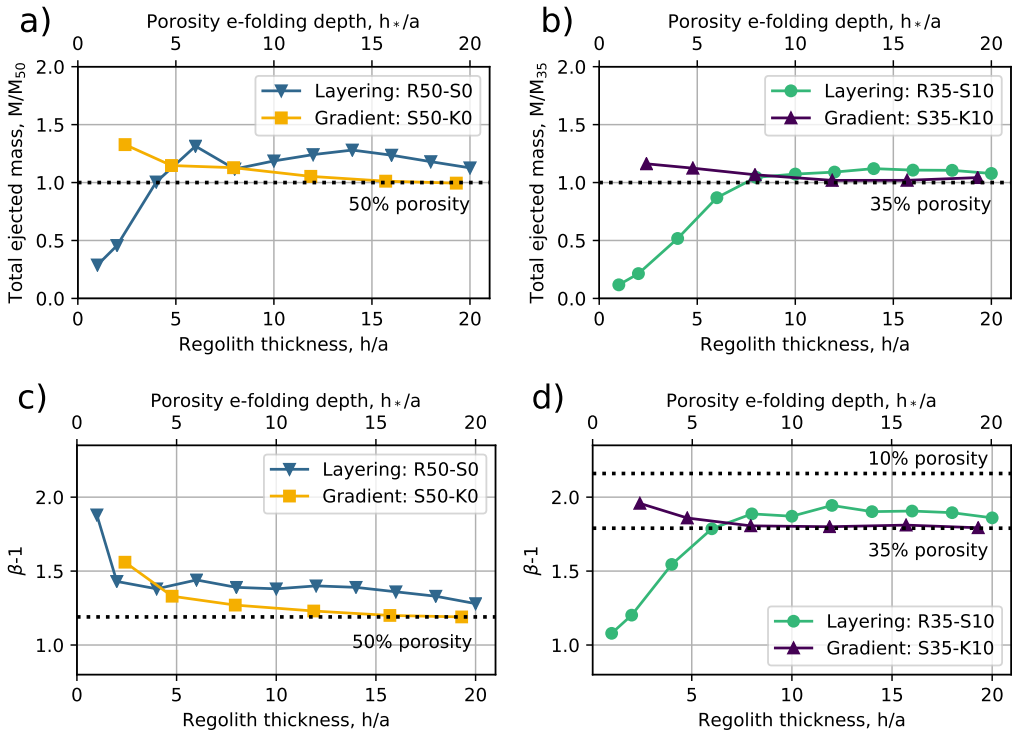

Figure 11: a) Total ejected mass, M, normalised by the ejected mass in the 50% porosity half-space scenario, M_{50}, as a function of regolith layer thickness, h/a, for R50-S0 and S50-K0 target scenarios. b) Total ejected mass normalised by the mass ejected in the 35% half-space scenario, M/M_{35}, as a function of regolith layer thickness, h/a, for R35-S10 and S35-K10 target scenarios. c) Normalised ejected momentum, $\beta - 1$, as a function of regolith thickness, h/a, for R50-S0 and S50-K0 target scenarios. d) $\beta - 1$, as a function of regolith thickness, for R35-S10 and S35-K10 target scenarios. In all figures, the upper label shows the equivalent porosity e-folding depth, h_*/a. The equivalent ejected mass and $\beta - 1$ for the porous half-space scenarios, are plotted for comparison (dotted lines).

4.2. Implications for the DART mission

The DART mission will be the first to produce a controlled deflection of a near-Earth asteroid. DART will provide a great opportunity to test our capability to deflect a potentially hazardous asteroid and to calibrate numerical simulations of m-scale impacts on asteroids.

The numerical simulations presented here used impactor properties appropriate for the DART spacecraft and target scenarios consistent with our current understanding of DART's target, Didymoon. In all of the target scenarios simulated, the deflection caused by the DART impact was amplified by the escaping crater ejecta; i.e., $\beta - 1 > 0$.

In this work we have shown that $\beta - 1$ can vary significantly depending on the target asteroid's properties and structure. If the DART spacecraft impacts a homogeneous porous target, we found that $\beta - 1$ can have values between 0.5 and 3.5, depending on the target cohesion and porosity. On the other hand, if the DART spacecraft impacts a layered target, the deflection can be both amplified by up to 30% or reduced by up to 60%, compared with the equivalent homogeneous upper layer case. If the transition between the surface material and the substrate is gradual, then $\beta - 1$ can be amplified by up to 30% compared with the case of a homogeneous high-porosity subsurface.

Our results also show that some of our simulated impacts into different targets produced very similar $\beta - 1$ values, yet very different crater sizes and morphologies. For example, the same deflection amplification ($\beta - 1 \approx 1.9$) was found when impacting homogeneous targets with cohesions and porosities of: 100 kPa and few percent porosity, 10 kPa and 20% porosity,

1 kPa and $\approx 30\%$ porosity or 0.1 kPa and $\approx 50\%$ porosity. Meanwhile, the same impacts produced craters that had radii of 5 m, 15 m, 23 m and 37 m, respectively.

The same amplification, $\beta - 1 \approx 1.9$, was also produced in different layered-target scenarios: An impact into a 50% porous regolith layer, one impactor radius thick, overlying a non-porous substrate produced a concentric crater with a radius of 4 m, while an impact into a regolith layer eight impactor radii thick, overlying a non-porous or few percent ($< 10\%$) porous substrate, produced a flat-floor crater, with a radius of ≈10 m. $\beta - 1 \approx 1.9$ was also observed in the simulations of impacts into targets in which porosity decreased exponentially with depth from a porosity of 35% at the surface to a minimum subsurface porosity of 10% at a depth of ≈ 1–2 m, which produced bowl shaped craters with radii of about 10 m.

Therefore, before the arrival of Hera at Didymoon, which will be able to evaluate the outcome of the DART impact in great detail, measurements of $\beta-1$ alone will not be sufficient for the purpose of numerical model validation. Data collected by the Hera spacecraft will be used to construct a shape model of Didymoon and constrain its bulk density, as well as setting approximate limits on the surface cohesion by surveying the asteroid surface roughness and performing a CubeSat bouncing experiment (Küppers et al., 2019). In addition, high-resolution images of the DART impact crater will determine the crater size and morphology.

Validation of numerical models of impact deflection against a controlled impact scenario with a measured $\beta - 1$ value is not only important for planetary defence, but also for inferring the subsurface structure of small aster-

oids. The DART crater morphology can provide insight into the surface and subsurface properties of Didymoon, whilst helping our understanding of the origins and formation processes of small near-Earth binary asteroids.

5. Conclusions

We conducted numerical simulations of the DART impact using the iSALE shock physics code. We investigated various different impact scenarios in the strength regime, to determine the sensitivity of crater morphology, ejecta mass-velocity distribution and momentum enhancement, β, to target properties and structure. Targets with three different structures were investigated: homogeneous porous half-space, layered targets with a porous weak upper layer overlying a stronger bedrock layer and targets with porosity that decreased exponentially with depth.

For impacts into homogeneous porous half-space, we found that cohesion has the greatest influence on crater diameter, while both cohesion and porosity have a major influence on the ejected mass and subsequently, the amount of momentum transferred from the impact for deflection. For the DART impact, the expected deflection was calculated $\beta - 1$ between 1 and 3, implying a momentum multiplication factor of between 2 and 4.

For impacts into layered targets, we found that that the presence of a less porous, stronger lower layer within six impactor diameters of the surface can influence the crater morphology and the mass velocity distribution of ejecta. We showed that there is an amplification in the amount of ejected mass, caused by the proximity of the stronger substrate to the surface and that the change in mass and velocity of the material ejected is dependent on

the thickness of the upper layer. However, this amplification does not always result in an enhancement of ejected momentum relative to the homogeneous upper-layer case. Both amplification and reduction of ejected mass and momentum relative to the homogeneous upper-layer case can occur in two-layer targets. This result has important implications for asteroid deflection. For the case of DART, momentum enhancement can change by up to 90%.

Impacts into targets with an exponentially decreasing porosity with depth produced an enhancement in the ejected mass and ejected momentum, but the effects were only considerable for relatively sharp decreases in porosity that occur within 6 m of the asteroid surface.

By measuring the DART crater, the Hera mission will provide vital data to test the predictive capabilities of numerical simulations of asteroid deflection.

6. Acknowledgements

We gratefully acknowledge the developers of iSALE-2D (www.isale-code.de), including Kai Wünnemann, Dirk Elbeshausen, Boris Ivanov and Jay Melosh. This work was funded by Science and Technology Facilities Council (STFC) (Grant ST/N000803/1).

7. References

Ahrens, T. J., Cole, D. M., 1974. Shock compression and adiabatic release of lunar fines from Apollo 17. Lunar and Planetary Science Conference Proceedings 3, 2333.

Ahrens, T. J., Harris, A. W., 1992. Deflection and fragmentation of near-Earth asteroids. Nature 360 (6403), 429–433.

Amsden, A., Ruppel, H., Hirt, C., 1980. SALE: a simplified ALE computer program for fluid flow at all speeds. Tech. Rep. LA-8095, 5176006.

Barnouin-Jha, O. S., Cheng, A. F., Mukai, T., Abe, S., Hirata, N., Nakamura, R., Gaskell, R. W., Saito, J., Clark, B. E., 2008. Small-scale topography of 25143 Itokawa from the Hayabusa laser altimeter. Icarus 198 (1), 108–124.

Benz, W., Asphaug, E., 1999. Catastrophic Disruptions Revisited. Icarus 142 (1), 5–20.

Bruck Syal, M., Michael Owen, J., Miller, P. L., 2016. Deflection by kinetic impact: Sensitivity to asteroid properties. Icarus 269, 50–61.

745 Cheng, A. F., Izenberg, N., Chapman, C. R., Zuber, M. T., 2002. Ponded
746 deposits on asteroid 433 Eros. Meteoritics & Planetary Science Archives
747 37 (8), 1095–1105.

748 Cheng, A. F., Michel, P., Jutzi, M., Rivkin, A. S., Stickle, A., Barnouin,
749 O., Ernst, C., Atchison, J., Pravec, P., Richardson, D. C., 2016. Asteroid
750 Impact & Deflection Assessment mission: Kinetic impactor. Planetary and
751 Space Science 121, 27–35.

752 Cheng, A. F., Rivkin, A. S., Michel, P., Atchison, J., Barnouin, O., Benner,
753 L., Chabot, N. L., Ernst, C., Fahnestock, E. G., Kueppers, M., Pravec, P.,
754 Rainey, E., Richardson, D. C., Stickle, A. M., Thomas, C., 2018. AIDA
755 DART asteroid deflection test: Planetary defense and science objectives.
756 Planetary and Space Science 157, 104–115.

757 Collins, G. S., Melosh, H. J., Ivanov, B. A., 2004. Modeling damage and
758 deformation in impact simulations. Meteoritics & Planetary Science 39 (2),
759 217–231.

760 Collins, G. S., Melosh, H. J., Wünnemann, K., 2011. Improvements to the
761 epsilon-alpha porous compaction model for simulating impacts into high-
762 porosity solar system objects. International Journal of Impact Engineering
763 38 (6), 434–439.

764 Colwell, J. E., Batiste, S., Hornyi, M., Robertson, S., Sture, S., 2007. Lunar
765 surface: Dust dynamics and regolith mechanics. Reviews of Geophysics
766 45 (2).

767 Coradini, A., Capaccioni, F., Erard, S., Arnold, G., De Sanctis, M. C., Fi-
768 lacchione, G., Tosi, F., Barucci, M. A., Capria, M. T., Ammannito, E.,
769 Grassi, D., Piccioni, G., Giuppi, S., Bellucci, G., Benkhoff, J., Bibring,
770 J. P., Blanco, A., Blecka, M., Bockelee-Morvan, D., Carraro, F., Carlson,
771 R., Carsenty, U., Cerroni, P., Colangeli, L., Combes, M., Combi, M., Cro-
772 visier, J., Drossart, P., Encrenaz, E. T., Federico, C., Fink, U., Fonti, S.,
773 Giacomini, L., Ip, W. H., Jaumann, R., Kuehrt, E., Langevin, Y., Magni,
774 G., McCord, T., Mennella, V., Mottola, S., Neukum, G., Orofino, V.,
775 Palumbo, P., Schade, U., Schmitt, B., Taylor, F., Tiphene, D., Tozzi, G.,
776 2011. The Surface Composition and Temperature of Asteroid 21 Lutetia
777 As Observed by Rosetta/VIRTIS. Science 334 (6055), 492–494.

778 Davison, T. M., Collins, G. S., Bland, P. A., 2016. Mesoscale modeling of im-
779 pact compaction of primitive solar system solids. The Astrophysical Jour-
780 nal 821 (1), 68.

781 Delbo, M., Libourel, G., Wilkerson, J., Murdoch, N., Michel, P., Ramesh,
782 K. T., Ganino, C., Verati, C., Marchi, S., 2014. Thermal fatigue as the
783 origin of regolith on small asteroids. Nature 508 (7495), 233–236.

784 Durda, D. D., Bottke, W. F., Enke, B. L., Merline, W. J., Asphaug, E.,
785 Richardson, D. C., Leinhardt, Z. M., 2004. The formation of asteroid
786 satellites in large impacts: results from numerical simulations. Icarus 170,
787 243–257.

788 Fujiwara, A., Kawaguchi, J., Yeomans, D. K., Abe, M., Mukai, T., Okada,
789 T., Saito, J., Yano, H., Yoshikawa, M., Scheeres, D. J., Barnouin-Jha,
790 O., Cheng, A. F., Demura, H., Gaskell, R. W., Hirata, N., Ikeda, H.,

791 Kominato, T., Miyamoto, H., Nakamura, A. M., Nakamura, R., Sasaki,
792 S., Uesugi, K., Jun. 2006. The Rubble-Pile Asteroid Itokawa as Observed
793 by Hayabusa. Science 312 (5778), 1330–1334.

794 Goodman, R., 1989. Introduction to Rock Mechanics. Wiley.

795 Gundlach, B., Blum, J., 2013. A new method to determine the grain size of
796 planetary regolith. Icarus 223 (1), 479–492.

797 Hagerty, M. M., Hite, D. R., Ullrich, C. R., J., H. D., 1993. One-Dimensional
798 High-Pressure Compression of Granular Media. Journal of Geotechnical
799 Engineering 119 (1), 1–18.

800 Holsapple, K. A., Housen, K. R., 2012. Momentum transfer in asteroid im-
801 pacts. I. Theory and scaling. Icarus 221 (2), 875–887.

802 Housen, K. R., Holsapple, K. A., 2003. Impact cratering on porous asteroids.
803 Icarus 163 (1), 102–119.

804 Housen, K. R., Holsapple, K. A., 2011. Ejecta from impact craters. Icarus
805 211 (1), 856–875.

806 Housen, K. R., Schmidt, R. M., Holsapple, K. A., 1983. Crater ejecta scal-
807 ing laws: Fundamental forms based on dimensional analysis. Journal of
808 Geophysical Research: Solid Earth 88 (B3), 2485–2499.

809 Housen, K. R., Sweet, W. J., Holsapple, K. A., 2018. Impacts into porous
810 asteroids. Icarus 300, 72–96.

811 Ivanov, B. A., Artemieva, N. A., 2002. Numerical modeling of the formation
812 of large impact craters. In: Special Paper 356: Catastrophic events and

mass extinctions: impacts and beyond. Vol. 356. Geological Society of America, pp. 619–630.

Ivanov, B. A., Deniem, D., Neukum, G., 1997. Implementation of dynamic strength models into 2d hydrocodes: Applications for atmospheric breakup and impact cratering. International Journal of Impact Engineering 20 (1), 411–430.

Ivanov, B. A., Melosh, H. J., Pierazzo, E., 2010. Basin-forming impacts: Reconnaissance modeling. Geological Society of America Special Papers 465, 29–49.

Jacobson, S. A., Scheeres, D. J., 2011. Dynamics of rotationally fissioned asteroids: Source of observed small asteroid systems. Icarus 214 (1), 161–178.

Johnson, G. R., Cook, W. H., 1983. A constitutive model and data for metals subjected to large strains, high strain rates and high temperatures. Proceedings of the 7th International Symposium on Ballistics, The Hague, 541–547.

Jutzi, M., Michel, P., 2014. Hypervelocity impacts on asteroids and momentum transfer I. Numerical simulations using porous targets. Icarus 229, 247–253.

Küppers, M., Michel, P., Carnelli, I., Ulamec, S., Abell, P. A., the Hera team, 2019. Hera – the european contribution to the first asteroid deflection demonstration. Lunar and Planetary Science, L, 2567.

835 Lauretta, D. S., DellaGiustina, D. N., Bennett, C. A., Golish, D. R., Becker,
836 K. J., Balram-Knutson, S. S., Barnouin, O. S., Becker, T. L., Bottke,
837 W. F., Boynton, W. V., Campins, H., Clark, B. E., Connolly, H. C.,
838 dAubigny, C. Y. D., Dworkin, J. P., Emery, J. P., Enos, H. L., Hamil-
839 ton, V. E., Hergenrother, C. W., Howell, E. S., Izawa, M. R. M., Kaplan,
840 H. H., Nolan, M. C., Rizk, B., Roper, H. L., Scheeres, D. J., Smith, P. H.,
841 Walsh, K. J., Wolner, C. W. V., 2019. The unexpected surface of asteroid
842 (101955) Bennu. Nature 568 (7750), 55.

843 Lundborg, N., 1967. The strength-size relation of granite. International Jour-
844 nal of Rock Mechanics and Mining Sciences & Geomechanics Abstracts
845 4 (3), 269–272.

846 Luther, R., Zhu, M.-H., Collins, G., Wünnemann, K., 2018. Effect of target
847 properties and impact velocity on ejection dynamics and ejecta deposition.
848 Meteoritics & Planetary Science 53 (8), 1705–1732.

849 McKay, D. S., Heiken, G., Basu, A., Blanford, G., Simon, S., Reedy, R.,
850 French, B. M., Papike, J., 1991. The lunar regolith, in The Lunar Source-
851 book. Cambridge Univ. Press, New York.

852 Melosh, H. J., Nemchinov, I. V., Zetzer, Y. I., 1994. Non-nuclear strategies
853 for deflecting comets and asteroids. pp. 1111–1132.

854 Michel, P., Benz, W., Tanga, P., Richardson, D. C., 2001. Collisions and
855 Gravitational Reaccumulation: Forming Asteroid Families and Satellites.
856 Science 294 (5547), 1696–1700.

Michel, P., Cheng, A., Küppers, M., Pravec, P., Blum, J., Delbo, M., Green, S., Rosenblatt, P., Tsiganis, K., Vincent, J., Biele, J., Ciarletti, V., Hérique, A., Ulamec, S., Carnelli, I., Galvez, A., Benner, L., Naidu, S., Barnouin, O., Richardson, D., Rivkin, A., Scheirich, P., Moskovitz, N., Thirouin, A., Schwartz, S., Campo Bagatin, A., Yu, Y., 2016. Science case for the asteroid impact mission (aim): A component of the asteroid impact & deflection assessment (aida) mission. Advances in Space Research 57 (12), 2529 – 2547.

Michel, P., Kueppers, M., Sierks, H., Carnelli, I., Cheng, A. F., Mellab, K., Granvik, M., Kestil, A., Kohout, T., Muinonen, K., Nsil, A., Penttila, A., Tikka, T., Tortora, P., Ciarletti, V., Hrique, A., Murdoch, N., Asphaug, E., Rivkin, A., Barnouin, O., Bagatin, A. C., Pravec, P., Richardson, D. C., Schwartz, S. R., Tsiganis, K., Ulamec, S., Karatekin, O., 2018. European component of the AIDA mission to a binary asteroid: Characterization and interpretation of the impact of the DART mission. Advances in Space Research 62 (8), 2261–2272.

Mitchell, J. K. H., 1974. Apollo soil mechanics experiment S-200, nasa contract nas 9-11266, space sciences laboratory. Tech. rep.

Miyamoto, H., Yano, H., Scheeres, D. J., Abe, S., Barnouin-Jha, O., Cheng, A. F., Demura, H., Gaskell, R. W., Hirata, N., Ishiguro, M., Michikami, T., Nakamura, A. M., Nakamura, R., Saito, J., Sasaki, S., 2007. Regolith Migration and Sorting on Asteroid Itokawa. Science 316 (5827), 1011–1014.

Murdoch, N., Hempel, S., Pou, L., Cadu, A., Garcia, R. F., Mimoun, D., Margerin, L., Karatekin, O., 2017. Probing the internal structure of the

asteriod Didymoon with a passive seismic investigation. Planetary and Space Science 144, 89–105.

Murdoch, N., Sanchez, P., Schwartz, S. R., Miyamoto, H., 2015. Asteroid Surface Geophysics. Asteroids IV, Patrick Michel, Francesca E. DeMeo, and William F. Bottke (eds.), University of Arizona Press, Tucson.

Nakamura, A. M., Hiraoka, K., Yamashita, Y., Machii, N., Feb. 2009. Collisional disruption experiments of porous targets. Planetary and Space Science 57 (2), 111–118.

Oberbeck, V. R., 1975. The role of ballistic erosion and sedimentation in lunar stratigraphy. Reviews of Geophysics 13 (2), 337–362.

Oberbeck, V. R., Quaide, W. L., 1967. Estimated thickness of a fragmental surface layer of Oceanus Procellarum. Journal of Geophysical Research 72 (18), 4697–4704.

Pierazzo, E., Artemieva, N., Asphaug, E., Baldwin, E. C., Cazamias, J., Coker, R., Collins, G. S., Crawford, D. A., Davison, T., Elbeshausen, D., Holsapple, K. A., Housen, K. R., Korycansky, D. G., Wünnemann, K., 2008. Validation of numerical codes for impact and explosion cratering: Impacts on strengthless and metal targets. Meteoritics & Planetary Science 43 (12), 1917–1938.

Prieur, N. C., Rolf, T., Luther, R., Wünnemann, K., Xiao, Z., Werner, S. C., 2017. The effect of target properties on transient crater scaling for simple craters. Journal of Geophysical Research: Planets 122 (8), 1704–1726.

Prieur, N. C., Rolf, T., Wünnemann, K., Werner, S. C., 2018. Formation of Simple Impact Craters in Layered Targets: Implications for Lunar Crater Morphology and Regolith Thickness. Journal of Geophysical Research: Planets 123 (6), 1555–1578.

Quaide, W. L., Oberbeck, V. R., 1968. Thickness determinations of the lunar surface layer from lunar impact craters. Journal of Geophysical Research 73 (16), 5247–5270.

Raducan, S. D., Davison, T. M., Luther, R., Collins, G. S., 2019. The role of asteroid strength, porosity and internal friction in impact momentum transfer. Icarus 329, 282–295.

Richardson, D. C., Leinhardt, Z. M., Melosh, H. J., Bottke, Jr., W. F., Asphaug, E., 2002. Gravitational Aggregates: Evidence and Evolution. In: Asteroids III. pp. 501–515.

Richardson, D. C., Michel, P., Walsh, K. J., Flynn, K. W., 2009. Numerical simulations of asteroids modelled as gravitational aggregates with cohesion. Planetary and Space Science 57 (2), 183–192.

Sánchez, P., Scheeres, D. J., 2014. The strength of regolith and rubble pile asteroids. Meteoritics & Planetary Science 49 (5), 788–811.

Scheeres, D. J., Hartzell, C. M., Sanchez, P., Swift, M., 2010. Scaling forces to asteroid surfaces: The role of cohesion. Icarus 210 (2), 968–984.

Schultz, P. H., 1992. Atmospheric effects on ejecta emplacement. Journal of Geophysical Research: Planets 97 (E7), 11623–11662.

925 Senft, L. E., Stewart, S. T., 2007. Modeling impact cratering in layered
926 surfaces. Journal of Geophysical Research: Planets 112 (E11), E11002.

927 Shafer, B. P., Garcia, M. D., Scammon, R. J., Snell, C. M., Stellingwerf,
928 R. F., Remo, J. L., Managan, R. A., Rosenkilde, C. E., 1994. The Coupling
929 of Energy to Asteroids and Comets. In: Gehrels, T., Matthews, M. S.,
930 Schumann, A. M. (Eds.), Hazards Due to Comets and Asteroids. p. 955.

931 Shoemaker, E. M., Gault, D. E., Moore, H. J., Lugn, R. V., 1963. Hyperve-
932 locity impact of steel into coconino sandstone. American Journal of Science
933 261 (7), 668–682.

934 Stephens, D. R., Lilley, E. M., 1970. Compressibilities of Lunar Crystalline
935 Rock, Microbreccia, and Fines to 40 Kilobars. Science 167 (3918), 731–732.

936 Stickle, A. M., Atchison, J. A., Barnouin, O. S., Cheng, A. F., Crawford,
937 D. A., Ernst, C. M., Fletcher, Z., Rivkin, A. S., 2015. Modeling Momentum
938 Transfer from Kinetic Impacts: Implications for Redirecting Asteroids.
939 Procedia Engineering 103, 577–584.

940 Sullivan, J. R., Thomas, C. P., Murchie, L. S., Robinson, S. M., 2002. Aster-
941 oid Geology from Galileo and NEAR Shoemaker Data. Asteroids III.

942 Tillotson, H. J., 1962. Metallic Equations of State for Hypervelocity Impact.
943 General Atomic Report GA-3216, 141.

944 Veverka, J., Farquhar, B., Robinson, M., Thomas, P., Murchie, S., Harch, A.,
945 Antreasian, P. G., Chesley, S. R., Miller, J. K., Jr, W. M. O., Williams,
946 B. G., Yeomans, D., Dunham, D., Heyler, G., Holdridge, M., Nelson,

947 R. L., Whittenburg, K. E., Ray, J. C., Carcich, B., Cheng, A., Chapman,
948 C., Iii, J. F. B., Bell, M., Bussey, B., Clark, B., Domingue, D., Gaffey,
949 M. J., Hawkins, E., Izenberg, N., Joseph, J., Kirk, R., Lucey, P., Malin,
950 M., McFadden, L., Merline, W. J., Peterson, C., Prockter, L., Warren,
951 J., Wellnitz, D., 2001. The landing of the NEAR-Shoemaker spacecraft on
952 asteroid 433 Eros. Nature 413 (6854), 390–393.

953 Vincent, J.-B., Besse, S., Marchi, S., Sierks, H., Massironi, M., Osiris
954 Team (A'Hearn, M., Barbieri, C., Barucci, A., Bertaux, J.-L., Cremonese,
955 G., Da Deppo, V., Davidsson, B., Debei, S., De Cecco, M., Fornasier, S.,
956 Fulle, M., Groussin, O., Gutierrez, P., Hviid, S., Ip, W.-H., Jorda, L.,
957 Keller, H., Koschny, D., Knollenberg, J., Kramm, J., Kuehrt, E., Lamy,
958 P., Lara, L., Lazzarin, M., Lopez-Moreno, J., Marzari, F., Michalik, H.,
959 Naletto, G., Rickman, H., Rodrigo, R., Sabau, L., Thomas, N., Wenzel.,
960 K.-P., Angrilli, F., 2012. Physical properties of craters on asteroid (21)
961 Lutetia. Planetary and Space Science 66, 79–86.

962 Walsh, K. J., Jawin, E. R., Ballouz, R.-L., Barnouin, O. S., Bierhaus, E. B.,
963 Connolly, H. C., Molaro, J. L., McCoy, T. J., Delbo, M., Hartzell, C. M.,
964 Pajola, M., Schwartz, S. R., Trang, D., Asphaug, E., Becker, K. J., Bed-
965 dingfield, C. B., Bennett, C. A., Bottke, W. F., Burke, K. N., Clark, B. C.,
966 Daly, M. G., DellaGiustina, D. N., Dworkin, J. P., Elder, C. M., Golish,
967 D. R., Hildebrand, A. R., Malhotra, R., Marshall, J., Michel, P., Nolan,
968 M. C., Perry, M. E., Rizk, B., Ryan, A., Sandford, S. A., Scheeres, D. J.,
969 Susorney, H. C. M., Thuillet, F., Lauretta, D. S., Apr. 2019. Craters,
970 boulders and regolith of (101955) Bennu indicative of an old and dynamic

surface. Nature Geoscience 12 (4), 242.

Walsh, K. J., Richardson, D. C., Michel, P., 2008. Rotational breakup as the origin of small binary asteroids. Nature 454 (7201), 188–191.

Walsh, K. J., Richardson, D. C., Michel, P., 2012. Spin-up of rubble-pile asteroids: Disruption, satellite formation, and equilibrium shapes. Icarus 220 (2), 514–529.

Watanabe, S., Hirabayashi, M., Hirata, N., Hirata, N., Noguchi, R., Shimaki, Y., Ikeda, H., Tatsumi, E., Yoshikawa, M., Kikuchi, S., Yabuta, H., Nakamura, T., Tachibana, S., Ishihara, Y., Morota, T., Kitazato, K., Sakatani, N., Matsumoto, K., Wada, K., Senshu, H., Honda, C., Michikami, T., Takeuchi, H., Kouyama, T., Honda, R., Kameda, S., Fuse, T., Miyamoto, H., Komatsu, G., Sugita, S., Okada, T., Namiki, N., Arakawa, M., Ishiguro, M., Abe, M., Gaskell, R., Palmer, E., Barnouin, O. S., Michel, P., French, A. S., McMahon, J. W., Scheeres, D. J., Abell, P. A., Yamamoto, Y., Tanaka, S., Shirai, K., Matsuoka, M., Yamada, M., Yokota, Y., Suzuki, H., Yoshioka, K., Cho, Y., Tanaka, S., Nishikawa, N., Sugiyama, T., Kikuchi, H., Hemmi, R., Yamaguchi, T., Ogawa, N., Ono, G., Mimasu, Y., Yoshikawa, K., Takahashi, T., Takei, Y., Fujii, A., Hirose, C., Iwata, T., Hayakawa, M., Hosoda, S., Mori, O., Sawada, H., Shimada, T., Soldini, S., Yano, H., Tsukizaki, R., Ozaki, M., Iijima, Y., Ogawa, K., Fujimoto, M., Ho, T.-M., Moussi, A., Jaumann, R., Bibring, J.-P., Krause, C., Terui, F., Saiki, T., Nakazawa, S., Tsuda, Y., 2019. Hayabusa2 arrives at the carbonaceous asteroid 162173 RyuguA spinning topshaped rubble pile. Science 364 (6437), 268–272.

995 Wilcox, B. B., Robinson, M. S., Thomas, P. C., Hawke, B. R., 2005. Con-
996 straints on the depth and variability of the lunar regolith. Meteoritics &
997 Planetary Science 40 (5), 695–710.

998 Wünnemann, K., Collins, G. S., Melosh, H. J., 2006. A strain-based porosity
999 model for use in hydrocode simulations of impacts and implications for
1000 transient crater growth in porous targets. Icarus 180 (2), 514–527.

1001 Wünnemann, K., Zhu, M.-H., Stöffler, D., 2016. Impacts into quartz sand:
1002 Crater formation, shock metamorphism, and ejecta distribution in labora-
1003 tory experiments and numerical models. Meteoritics & Planetary Science
1004 51 (10), 1762–1794.

1005 Yano, H., Kubota, T., Miyamoto, H., Okada, T., Scheeres, D., Takagi, Y.,
1006 Yoshida, K., Abe, M., Abe, S., Barnouin-Jha, O., Fujiwara, A., Hasegawa,
1007 S., Hashimoto, T., Ishiguro, M., Kato, M., Kawaguchi, J., Mukai, T.,
1008 Saito, J., Sasaki, S., Yoshikawa, M., 2006. Touchdown of the Hayabusa
1009 Spacecraft at the Muses Sea on Itokawa. Science 312 (5778), 1350–1353.

Appendix A. Appendix

Additional supporting information (tables, model outcomes) will be provided at the time of the publication as a DOI.